Results in Engineering 29 (2026) 109591

Contents lists available at ScienceDirect

Results in Engineering

journal homepage: www.sciencedirect.com/journal/results-in-engineering

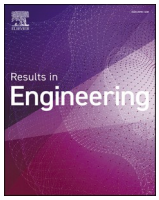

Research paper

High-quality freeform machining of chemically strengthened glass using spark assisted chemical engraving

Seyed Ali Delbari, Jean-Philippe Leclair, Guillaume Villeneuve, Lucas A. Hof *

Department of Mechanical Engineering, École de technologie supérieure, 1100 Notre-Dame Ouest, Montréal, Québec H3C 1K3, Canada.

ARTICLE INFO

Keywords:
Spark assisted chemical engraving
Chemically strengthened glass
Micro-machining
Gorilla glass 3
Non-conventional precision machining

ABSTRACT

This work demonstrates the first-ever utilization of Spark Assisted Chemical Engraving (SACE) for the freeform micro-machining of Chemically Strengthened Glass (CSG), achieving cut qualities that surpass existing laser and mechanical techniques for this notoriously difficult-to-process material. Using a Response Surface Methodology, the effects of key input parameters, voltage (33-37 V), cutting speed (5-15 μm/s), and electrolyte (KOH) concentration (24-30 wt.%), were investigated on critical output quality metrics, including chipping, cut surface roughness (S_a), and cut kerf. Statistical models were developed to predict outcomes, revealing complex parameter interactions including a synergistic effect between voltage and KOH concentration where high voltage degrades surface quality (especially at higher electrolyte concentrations). Among tested parameters, best results were achieved at 33 V, 5 μm/s and 30 wt.% KOH, resulting in superior surface integrity ($S_a \approx 2.41$ μm, chipping size ≈ 4.1 μm). SACE is validated as a viable single-step freeform machining process for CSG, mitigating defects common in mechanical and laser-based methods, and provides a practical solution for remanufacturing high-value CSG waste within a circular economy framework.

1. Introduction

Glass has many applications in daily life, such as consumer electronic displays, architectural glazing, everyday packaging, and advanced optics, owing to its combination of properties such as transparency, hardness, and chemical inertness [1]. A transition from the traditional linear economy to a circular economy for glass is important for several reasons: the glass industry is highly energy-intensive [2], glass production results in significant emissions of combustion gases, such as CO_2 [3], glass is non-biodegradable [4], and large amounts of glass waste are produced daily due to its broad range of applications [5]. Chemically Strengthened Glass (CSG) waste, primarily used in smartphone screens, can be one of the most challenging types to handle because of its wide range of compositions [6,7]. Additionally, the presence of a high level of surface compressive stress makes it very challenging to re-machine, especially by conventional techniques, for use in alternative applications as a revalorization strategy [8].

However, the literature reports a few endeavors to machine CSGs using mostly laser-based advanced machining techniques. Ogi et al. [9] and Furumoto et al. [8] used a fracture control technique to cut a CSG. In their work, they first used laser beam irradiation to apply a thermal shock, creating an initial crack. The presence of thermal stress inside the glass helped this crack propagate in the direction of a prefabricated groove via a short-pulsed laser on the glass surface to facilitate the cutting and separation of the CSG. The quality of the cleaved surface was highly dependent on the quality of the initial groove, and the best results in the latter were reported for grooves fabricated using a short-pulsed diode-pumped solid-state laser, which could prevent the formation of thermal damage such as lateral or median cracks. Park et al. [10] utilized a femtosecond laser to create sub-surface cracks in CSG to cut it without damage. In this practice, the laser beam was focused on a certain depth, melting the glass. The driving force for crack formation was the tensile stress around that focal spot due to the re-solidification and rearrangement of the glass structure. The path of the laser, along with carefully controlled parameters such as power, pulse peak intensity, pulse repetition rate, feed speed, focal depth, focal spot size, etc., guided the crack propagation. In another laser deployed strategy, Chuang et al. [11] combined laser ablation with thermo-shock quenching to cut interior holes in CSGs. After creating micro-trenches with ~2 μm diameter by a picosecond laser, the glass was heated up to 200-250°C and subsequently quenched by CHF_3 jets at -80°C. This thermal shock provided enough tensile stress for crack propagation from

* Corresponding author.
E-mail address: lucas.hof@etsmtl.ca (L.A. Hof).

https://doi.org/10.1016/j.rineng.2026.109591
Received 29 January 2026; Received in revised form 12 February 2026; Accepted 12 February 2026
Available online 13 February 2026

micro-trenches, resulting in glass cutting. Poor cleavage surface and random chipping on the cut edges were two main issues in this approach.

Apart from laser-based techniques, some other researchers have tried to find alternative solutions for CSG machining. For example, Noma et al. [12] deployed axial ultrasonic-vibration-assisted helical milling to create micro through-holes with improved machining accuracy, minimized chipping, and reduced tool wear. Their results showed that axial ultrasonic vibration led to intermittent cutting, which enhanced cutting fluid flow, improved chip evacuation, and resulted in smoother drilling. Moreover, compared to conventional helical milling, using ultrasonic vibration reduced thrust force, consequently reducing chipping, tool breakage, and tool wear. Under optimum milling conditions, chipping size was reduced by 86% at the outlet (from 509 μm to 72.2 μm) and 41% at the inlet (from 82.7 μm to 49.0 μm) of the holes, respectively, compared to the conventional technique. However, the cut quality was still poor due to the presence of random chipping. Also, Mizobuchi et al. [13] designed an electroplated diamond tool to improve the performance and quality of CSG drilling. The tool's shank was made of cemented carbide with a single layer of synthetic diamond abrasive grains electroplated with nickel. To improve chip ejection during drilling, the sides of the cylindrical tool were partially removed. However, although this custom-designed tool could successfully drill through-holes in CSGs without applied vibration, chipping, especially on the outlet side, was significant. On the inlet side, the edge quality was also poorer compared to similar research works using ultrasonic vibration. Overall, it can be stated that the main issues in CSG machining, such as chipping and tool wear, stem from the surface compression layer, which necessitates applying thrust force in conventional techniques. This force can create high levels of tensile stress at the outlet of machined holes, resulting in poor machining edges [14].

To address this issue, Kim et al. [15] proposed an approach combining electrochemical discharge (ECD) and grinding processes. This technique consisted of four stages: (1) reverse ion exchange, replacing K^+ ions with Na^+ ions on the glass surface using an electrolyte solution containing Na^+ ions and a blade-shaped electrode to create localized discharge to facilitate reverse ion exchange via the ECD process; (2) grinding to the lower compression stress layer; (3) a second ECD process to remove the lower compression stress layer; and (4) a final grinding process. Although the cut quality of this process appears better than that of the previously elaborated techniques, and the authors claimed that this technique is more cost-effective compared to laser-based technologies, the process is still very time-consuming. Moreover, it is not well-suited for, and indeed may be incapable of producing, cuts with complex or non-linear shapes.

While the freeform machining of brittle materials like glass has been widely investigated [16,17], the limitations of existing techniques for CSG necessitate a different approach. As a viable alternative solution intended to overcome the limitations of complex, multi-step, and poor-quality techniques, Spark Assisted Chemical Engraving (SACE) emerges as a promising process that utilizes a hybrid thermochemical mechanism appropriate for the high-precision micromachining of glass [18,19]. This technique requires the submersion of the glass sample in an electrolyte, such as potassium hydroxide (KOH) or sodium hydroxide (NaOH), and the application of a voltage between a tool-electrode and counter-electrode. Above a critical voltage, electrolysis results in the formation of an insulating gas film around the tool, which enables localized electrical discharges (sparks) that facilitate material removal through combined thermal and chemical etching, thereby allowing the fabrication of micro-features like holes, channels, and cuts for applications ranging from microfluidics to personalized consumer electronics parts [20,21].

Although researchers have investigated various laser, mechanical, and hybrid techniques for machining CSGs, the consistent achievement of high-quality cuts free from chipping and with arbitrary geometric freedom remains a significant obstacle. Issues such as extensive edge chipping, poor surface quality, potential thermal damage, and process complexity or lengthy processing times frequently compromise the outcomes, largely owing to the challenges posed by the high surface compressive stress inherent in CSGs. These methods either demonstrate an inability to adequately manage the complex stress profile of the material, which leads to uncontrolled fracture and chipping, or are too geometrically constrained to produce complex shapes. Therefore, the investigation of alternative single-step processes capable of precise freeform material removal without inducing mechanical stress is essential, which suggests that the SACE process is a potentially effective approach in this domain.

This study presents a novel manufacturing milestone: the first-ever direct application of SACE to micro-machine CSG. Unlike previous laser or mechanical attempts that struggle with the material's complex stress profile, this work demonstrates that SACE can produce freeform cuts with edge quality and surface integrity superior to currently available techniques. The primary focus is the investigation of SACE as a feasible, one-step approach to tackle the substantial machining problems of CSG with a specific focus on the commonly encountered chipping problem. The aim is to systematically analyze the relationships between the cutting quality of CSG and the operating parameters (voltage, cutting speed and electrolyte concentration) of the SACE process. A custom Response Surface Methodology (RSM) is utilized to demonstrate feasibility and identify key process parameters, establishing a novel approach for precision cutting of complex freeform shapes in CSG with low surface and material damage. Freeform denotes the capability to generate arbitrary 2.5D paths and complex planar shapes (contrasted with basic linear cuts or drilled holes). Such a capability presents a significant challenge due to the inherent machinability characteristics of CSGs, which increase for freeform geometries, thus positioning SACE as a viable option for upcycling high-value waste of CSG origin such as end-of-life smartphone screens into alternative applications. The overall structure and workflow of the present study are depicted schematically in Fig. 1.

2. Materials and methods

2.1. SACE setup and materials

This research utilized a custom-built, three-axis SACE machine, developed in-house at the Laboratory of Smart and Circular Manufacturing (LFIC) group at École de technologie supérieure (ÉTS), Montréal, Canada. The experimental apparatus is configured with a conductive tool-electrode (300 μm diameter), acting as the cathode, which is mounted via an ER-11 collet to a Dobtian WS55-140 spindle. The electrical potential for the process is supplied by a CHUX S-2000-48 DC power supply (0-90 V, 2 kW), and an Elditest CP6550 current probe is integrated into the circuit to monitor the electrical signal for process control. An SS316 sheet counter-electrode (anode) with a large surface area (200 cm^2, 25 mm × 800 mm) is used while the workpiece is submerged in KOH electrolyte (inter-electrode gap ~50 mm). Tool-electrode movement is governed by three Newport motion axes (ILS-150cc x/y, ILS-50cc z) with positioning accuracy of ±0.5 μm, and accurate tool-to-workpiece referencing is achieved via in-situ probing (tool-electrode acting as contact probe [22,23]). The experimental setup and SACE working principle (controlled electrical discharges and chemical reactions [24]) are illustrated in Fig. 2.

To isolate primary variables (voltage, speed, electrolyte concentration), constant process parameters are maintained, specifically a 300 μm diameter tungsten carbide (WC) tool electrode chosen for high wear resistance and electrical conductivity. Byproduct removal (e.g., K_2SiO_3, $KAlO_2$) from the narrow machining gap is facilitated by a twist-drill bit geometry (Fig. 3), while a constant counterclockwise (CCW) tool rotation (ω) of 800 rpm is applied to promote machining uniformity and circulate fresh electrolyte. Tool consistency was validated by post-experiment inspection via confocal microscope (no significant wear),

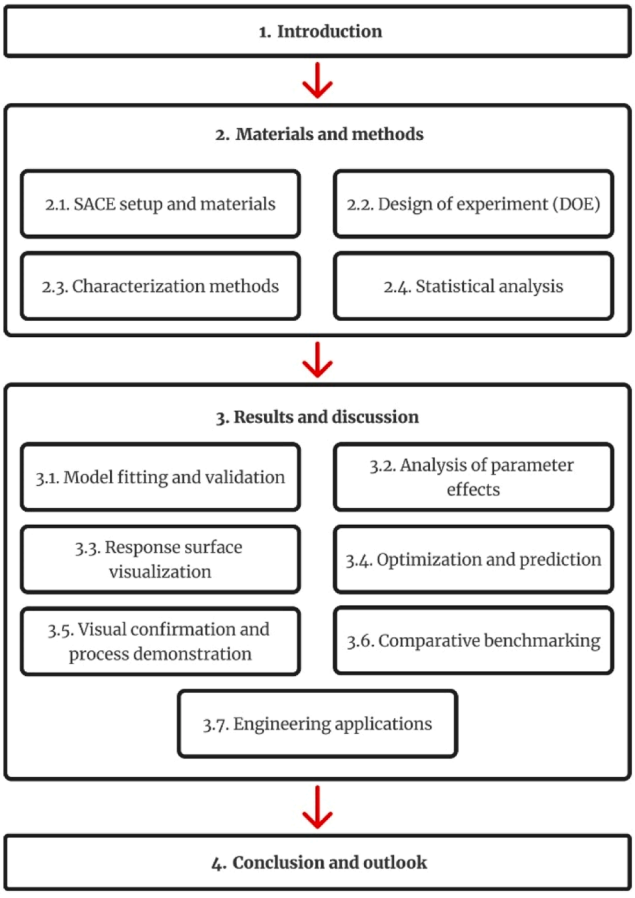

Fig. 1. Structure of the present study is illustrated schematically. Progression from the custom SACE setup and DOE to statistical analysis and final process optimization using RSM is detailed in the workflow.

and a steady electrolyte flow rate of 180 ml/min was maintained using a Masterflex Miniflex MFLA-77920-40 peristaltic pump (Table 1).

The workpiece material selected for this investigation was commercially available CSG, specifically Corning® Gorilla Glass 3 (GG3), purchased from Abrisa Technologies, USA. The schematic dimensions and residual stress profile of the as-received samples are shown in Fig. 4. The as-received samples had dimensions of 25 mm × 25 mm × 0.55 mm. Main material properties, including the surface compression stress and case depth, are provided in Table 2. Samples were submerged horizontally within the KOH electrolyte and held in place with clamping screws.

2.2. Design of experiment (DOE)

To assess the effect of SACE parameters on cut quality for GG3, an

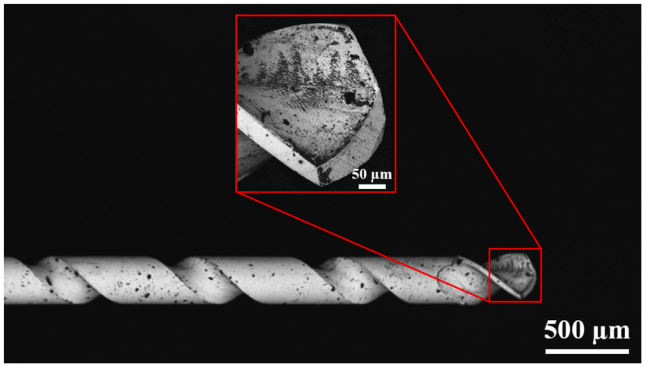

Fig. 3. Scanning Electron Microscope (SEM) image of the WC tool electrode employed in experiments is shown. Twist-drill bit geometry is featured on the 300 µm diameter tool to facilitate electrolyte circulation and byproduct evacuation from the narrow gap.

Table 1
Fixed SACE machining parameters and specifications used throughout the experiments are listed. Constants (including 800 rpm rotation and electrolyte flow rate) were selected to ensure stable conditions and facilitate electrolyte circulation while isolating variable effects of voltage, cutting speed, and KOH concentration.

Tool electrode material	Tungsten Carbide (WC)
Tool electrode diameter	300 µm
Tool electrode tip geometry	Twist-drill bit
Tool rotation	800 rpm
Counter Electrode	Stainless steel plate
Electrolyte flow rate	180 ml/min

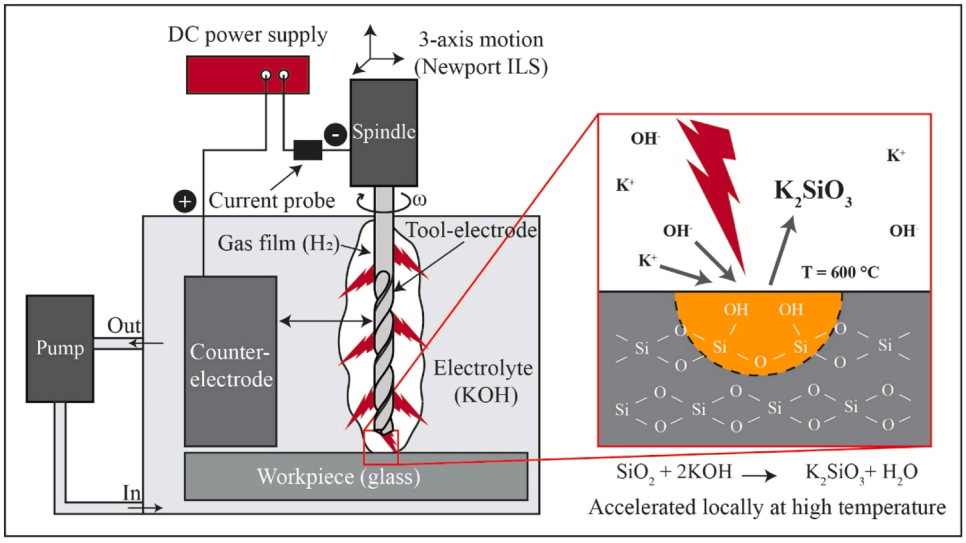

Fig. 2. Experimental setup and SACE process mechanism for glass machining are represented. Formation of an insulating hydrogen gas film around the tool-electrode is highlighted, enabling localized thermal discharges to accelerate chemical etching.

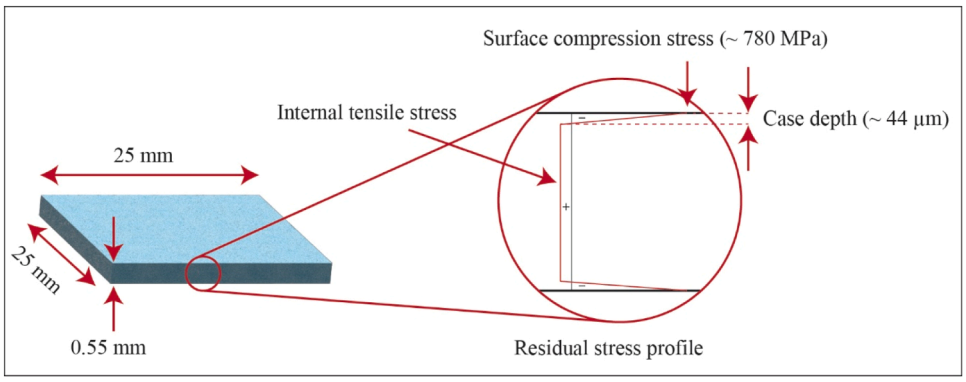

Fig. 4. Dimensions and stress profile of as-received GG3 samples are depicted. A critical case depth (~44 μm) and high surface compressive stress (~780 MPa) are identified, posing challenges for conventional machining.

Table 2
As-purchased GG3 specifications and residual stress profile are presented. Measured surface compressive stress of ~780 MPa and case depth of ~44 μm highlight the complex stress profile of the material, which creates significant challenges for conventional machining and necessitates the specialized SACE approach.

Dimensions	25 mm × 25 mm × 0.55 mm
Density	2.39 g/cm^3
Young's Modulus	70 GPa
Poisson's Ratio	0.22
Shear Modulus	28.5 GPa
Vickers Hardness (200g load), Strengthened	653 kgf/mm^2
Fracture Toughness	0.66 MPa m$^{0.5}$
Coefficient of Thermal Expansion (0-300°C)	75.8 × 10^{-7}/°C
Compressive Stress *	780.6 ± 1.4 MPa
Case Depth *	43.8 ± 3.1 μm

* *These values were measured by Abrisa Technologies using a commercial FSM-6000 device.*

RSM approach was utilized. Considering the challenges related to electrolyte changes between runs, which can introduce significant electrolyte concentration fluctuations, due to the remaining electrolyte in the piping system, and consequently experimental error, this study employed a custom RSM design incorporating a split-plot structure. This structure involved 5 whole plots, each maintaining a constant electrolyte (KOH) concentration, treated as a hard-to-change parameter. The experimental design was generated using the statistical software JMP (Ver. 18, SAS Institute, USA). The initial design consisted of 16 runs; however, to improve the robustness of the design and enhance model estimation, the total number of runs was increased to 32 by including random replications. The experimental parameters along with their tested levels, and the measured responses (see Section 2.3) with their units/categories, are presented in Table 3.

Parameter limits (Table 3) are selected based on literature, preliminary experiments, and process constraints. The KOH concentration center point (27 wt.%) is chosen near the maximum specific conductivity point [25], while the range (24-30 wt.%) encompasses values for effective SACE operation. A voltage range (33-37 V) is selected to ensure stable spark formation and enable micro-machining across all tested electrolyte concentrations, and the cutting speed range (5-15 μm/sec) is determined. It is important to note that "cutting speed" throughout this paper refers to the linear feed rate of the tool electrode. The upper limit represents the maximum feasible speed observed across all V-C combinations without causing tool breakage during preliminary tests. Subsequent statistical analysis, including model fitting and optimization, was also performed using JMP software (details in Section 2.4 and Section 3).

Table 3
Experimental design parameters with tested levels and measured responses are detailed. The design spans a voltage range of 33-37 V, a cutting speed of 5-10 μm/sec, and a KOH concentration of 24-30 wt.% to ensure stable spark formation, while responses were selected to evaluate geometric precision (SDI, cut kerf) and surface quality (chipping, S_a).

Category	Item	Type	Levels / Unit
Variables (parameters)	Voltage (V)	Continuous	33, 35, 37 V
	Cutting speed (S)	Continuous	5, 10, 15 μm/sec
	KOH concentration (C)	Continuous	24, 27, 30 wt. %
Responses	Chipping	Continuous	μm
	Cut kerf	Continuous	μm
	Surface distance index (SDI)	Continuous	Dimensionless ratio
	Cut surface roughness (S_a)	Continuous	μm
	Edge roundness	Continuous	μm
	Chipping severity	Ordinal	None, Occasional, Widespread

2.3. Characterization methods

To investigate SACE parameter impacts on cut quality, five quantitative responses (chipping, cut kerf, Surface Distance Index (SDI), S_a, edge roundness) and one qualitative response (chipping severity) are measured, addressing primary CSG machining challenges (minimizing edge damage, achieving high-quality surface finish) required for smartphone screen aesthetic appeal and structural integrity. Cut edges are analyzed from optical micrographs acquired using a Keyence VHX-7000 digital microscope (Keyence Co., Japan) and processed via ImageJ (Ver. 1.54p, USA), while topographical data is acquired using a Lext OLS4100 laser confocal microscope (Olympus Co., Japan) and analyzed using Lext software (Ver. 3.1.15, Japan) (see Fig. 5 for visualization).

- Chipping was quantified as the maximum perpendicular distance from the intended cut line to the edge of the worst observed chipping. To measure this, parallel lines (Fig. 5) were algorithmically fitted to the inner and outer cut edges, ensuring they were parallel to the cut itself. This perpendicular distance was then recorded.
- Cut kerf was determined from microscope images using the Fiji distribution of ImageJ. Parallel lines were fitted along the inner cut edges based on the high contrast between the glass surface and the void in the kerf, and the distance between the lines was recorded as the kerf width. This method was preferred to direct mechanical measurements, as it prevents damaging the fragile edges and provides a representative continuous measurement rather than discrete point values. Since the image analysis procedure is deterministic,

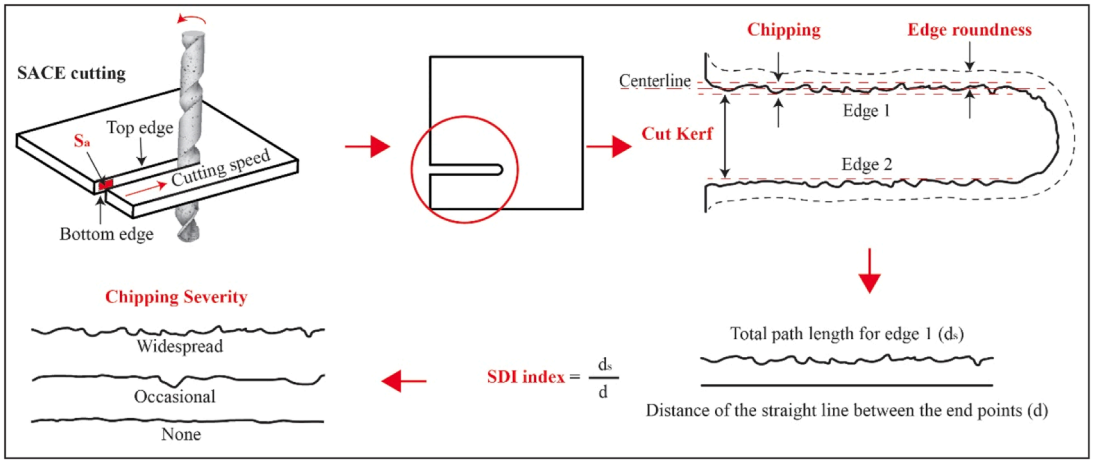

Fig. 5. Characterization methods and measured response definitions after SACE cutting are illustrated. Key metrics include SDI for cut straightness (ratio of actual path length to straight-line distance), chipping (quantified as maximum perpendicular distance from intended cut line to edge of the worst observed chipping), cut kerf (width of material removed), and edge roundness (sharpness defined by distance between the outside of the edge radius and the straight reference line). Additionally, chipping severity is categorized qualitatively (none, occasional, widespread), while S_a represents arithmetic average roughness of the exposed cut surface.

repeating the measurement on the same image yields identical results. The uncertainty is therefore mainly related to the image resolution and edge sharpness, which in our case corresponds to approximately one pixel.

- The SDI was measured as the proportion of the shortest straight-line distance between the endpoints of the cut edge and the actual total length [26]. This metric is a measure of the straightness of the cut path. A perfect, straight cut would have an SDI of 1, while a jagged or wavy cut path would have an SDI greater than 1. Therefore, a value closer to 1 indicates a higher quality, more precise cut.
- Edge roundness was measured optically, from the top view of the cut line. It was taken as the average (over 5 measurements) of the distance between the outside of the edge radius and the straight reference line. As illustrated in the schematic (Fig. 5), this reference line was the centerline, defined as a line parallel to and equidistant from the parallel lines fitted to the inner and outer cut edges.
- For measuring the arithmetic average surface roughness (S_a), the samples were carefully fractured to expose the cut surface. Topographical images from confocal microscope were analyzed using the Lext software, recording S_a values for at least 90% of the surface (~500 μm × 800 μm). The Lext software uses ISO 25178, applying an S-filter and an L-filter to separate roughness from waviness and errors.
- Finally, chipping severity was categorized qualitatively by visual inspection as none (no chipping), occasional (one or two chippings), and widespread (several observable chips). This ordinal scale was intended to complement the quantitative chipping measurement by capturing the overall distribution of edge defects. To ensure consistency and minimize observer bias, all qualitative assessments were performed by the same trained operator.

2.4. Statistical analysis

All statistical modelling and analysis were done using JMP software. Since there are two different response types (continuous and ordinal), different approaches were implemented for data analysis.

For the five continuous responses, quadratic RSM was formulated with the aim of understanding the relationships between different process parameters as well as their significance. This approach was selected due to its capability to assess possible curvature in the response surface and parameter interactions, which is common in physical processes like SACE [27]. Because the split-plot strategy kept KOH concentrations constant within whole plots, the Standard Least Squares technique is inappropriate as it fails to properly account for the variance associated with the whole plots (blocks) separately from the residual error [28]. Instead, a Restricted Maximum Likelihood (REML) approach was used to fit the models, which is preferred for mixed-effects models, including both fixed effects like V, S, C, their interactions, and random effects like the whole plots. REML provides unbiased estimates of variance components induced by blocking, making it possible to evaluate the variance contribution from whole plots. Additionally, the significance of the fixed-effect terms, including linear, quadratic, and interaction terms for V, S, and C parameters, was evaluated using Fixed Effect Tests (F-tests) within these REML models.

In contrast, an Ordinal Logistic Regression (OLR) model was employed for the chipping severity response with ordered levels (none < occasional < widespread). Designed to model cumulative probabilities for ordered categorical results (e.g., predicting the probability of observing chipping severity of occasional or less), this technique could not include the random whole plots effect. The omission likely had minimal impact on model validity as the whole plots contributed negligibly to variance (as detailed in Section 3.1). After this amendment, the statistical significance of other terms in influencing the chipping severity was evaluated using Effect Likelihood Ratio Tests. In such tests, the likelihood of two models—one with and one without a specific predictor (e.g., V term)—is compared, providing a Chi-Square statistic to assess the overall importance of that predictor. The Lack of Fit test was used to assess the Goodness-of-fit for the ordinal model, and the pseudo-R^2(U) metric was used to estimate the overall explanatory power.

Finally, the prediction profiler tool in JMP was used to identify desirable machining conditions considering all responses simultaneously. This powerful tool allows for interactive exploration of fitted models, and desirability functions can be employed to numerically search for parameter combinations to meet various objectives, e.g., minimizing chipping, minimizing edge roundness, and keeping cut kerf within limits.

3. Results and discussion

3.1. Model fitting and validation

Following the experimental runs and sample characterization, statistical models were developed to relate the SACE process parameters and their interactions to the measured responses. However, before

discussing the models and the significant parameters for each response, it is crucial to validate these models.

As discussed before, to prevent error inclusion due to the electrolyte change in each run, an REML estimation was implemented. The analysis indicated that the variance component related to the whole plots was negligible for all five continuous responses (Wald P>0.45). Excluding cut kerf, the estimated variance components for the whole plots were near zero for all others. In the case of cut kerf, the statistics showed a significant Wald p-value of 0.0185 associated with a negative variance estimate, likely resulting from an estimation process error when the actual variance is near zero. As a result, it can be stated that the overall impact of blocking was not significant. This outcome confirms that the primary source of variations were the fixed effects and residual errors.

The adequacy of the quadratic RSM fitted to continuous responses is presented in Table 4, where all models demonstrated statistical significance (P-value $\leq$ 0.0189 for chipping and P-value $<$ 0.0001 for others), suggesting the identified relationships are unlikely to arise from random chance. Moderate fits are observed for chipping (R^2Adj = 0.544) and cut kerf (R^2Adj = 0.579), common when machining brittle materials as inherent stochastic events contribute to significant unexplained variability, resulting in moderate predictive precision despite the models being statistically significant and valuable for understanding process trends.

In contrast, the models provided good fits for SDI (R^2Adj = 0.784) and edge roundness (R^2Adj = 0.799), and very good fit for S_a (R^2Adj = 0.868). For instance, the last fit suggests that the model explains approximately 87% of the variation in surface roughness. In addition, the Root Mean Square Error (RMSE) values provide an estimate of the typical prediction error for each response. Diagnostic checks, such as residual plots (Fig. A.1, Appendix A), showed reasonably random scatter around zero, indicating no major violations of model assumptions.

For the chipping severity response, as explained in Section 2.4, the OLR model was employed and the random effects from the whole plots were excluded from the model. The overall model demonstrated high significance with a Chi-Squared (χ^2) of 47.11 and P-value $<$ 0.0001, which confirms the ability of the model to predict the chipping severity level. Furthermore, the Lack of Fit test was non-significant (P-value = 1.0000), indicating that the model structure provides an adequate representation of the data trends. The model's explanatory power was substantial for this type of data, reflected by a pseudo-R^2(U) value of 0.795.

Finally, canonical analysis was performed on the fitted quadratic surfaces for the continuous responses to understand their curvature and locate stationary points, where the predicted gradient is zero. This analysis revealed saddle points for chipping, SDI, S_a, and edge roundness, and a theoretical minimum point for cut kerf. A critical finding, however, was that for all five continuous responses, the calculated stationary points lay outside the explored experimental range. This indicates that within the studied process window, the optimal conditions, e.g., lowest S_a, lowest chipping, are unlikely to occur at an interior combination of parameters but rather at the boundaries, i.e., at the lowest or highest settings of one or more parameters. This justified the subsequent use of the prediction profiler tool (introduced in Section 3.4) to explore the entire modeled response space, including the boundaries, for practical optimization.

Table 4
Model fit summary for continuous response surface models is provided. Analysis shows Good to Very Good fits for SDI, S_a and edge roundness, while Moderate fits for chipping and cut kerf reflect the inherent stochasticity and unpredictability of the process when machining brittle materials.

Response	R^2 Adj	RMSE	Model P-value	Fit Quality
Chipping (μm)	0.544	3.895	0.0189	Moderate
Cut Kerf (μm)	0.579	5.946	<0.0001	Moderate
SDI	0.784	0.009	0.0001	Good
Sa (μm)	0.868	0.294	<0.0001	Very Good
Edge Roundness (μm)	0.799	1.405	0.0001	Good

3.2. Analysis of parameter effects

Key insights into the SACE process for GG3 were revealed by evaluating the statistical significance (P-values) and the practical significance (i.e., the magnitude and direction of the effects) of each process parameter (voltage, speed, and KOH concentration) and its effects on the measured responses (chipping, cut kerf, SDI, S_a, and edge roundness). The statistical significance is outlined in Table 5, while the practical implications and trade-offs are best visualized using the interaction plots (this Section) and the prediction profiler (Section 3.4).

The most important factor was consistently voltage (P-value $<$ 0.001 for all responses), highlighting the critical role of electrical discharge intensity in SACE [18]. Beyond its statistical significance, voltage demonstrated the largest practical effect on most responses. For instance, experimental observations showed that increasing voltage led to a substantial and detrimental increase in chipping, cut kerf, and S_a, while only slightly improving (decreasing) edge roundness. This large effect size underscores that voltage is the primary control lever for the process, but its use must be carefully managed to avoid significant degradation in cut quality. Additionally, it significantly raised the likelihood of severe chipping (Ordinal P-value $<$ 0.0001). This is consistent with the knowledge from literature and observed by conducted experiments that increased voltage causes more frequent and intense discharges, which intensify thermal and chemical etching while simultaneously increasing surface imperfections [29]. Apart from the role of voltage increase on increasing Material Removal Rate (MRR), it can also enhance hydrogen bubble generation and consequently, improve the intensity of sparks [30]. This phenomenon can explain why higher voltage resulted in sharper edges and a decrease in cut edge roundness.

While statistically significant for SDI (P-value = 0.023*) and S_a (P-value = 0.008*), the practical effect of cutting speed is more nuanced and reveals important process trade-offs. For example, the tendency that faster machining speeds result in reduced S_a (smoother surface) at low/moderate voltages (Fig. A.2, Appendix A) may appear paradoxical but could be related to shorter interaction times per unit area, restricting the amount of surface etching irregularities. This advantage is offset, however, by an increase in SDI, i.e., less smooth edges. The magnitude of these changes, however, was observed to be considerably smaller than those caused by voltage, indicating that speed is a secondary parameter for fine-tuning rather than a primary driver of quality. The speed effect on ordinal chipping severity was not significant (P-value = 0.0625), unlike its quadratic term discussed below. Also, according to the statistical analysis of the experimental observations (Table 5), the linear effect of speed on cut kerf, chipping, and edge roundness is shown to be insignificant.

KOH concentration significantly impacted S_a (P-value = 0.008*), edge roundness (P-value = 0.004*), and chipping severity (P-value $<$ 0.0001*). Higher KOH concentrations accelerate etching [31], which could result in rougher surfaces (higher S_a) and increased chipping severity probability. More effective chemical activity may also be connected to a sharper edge (decreased edge roundness) [32]. The absence of a detectable linear influence on cut kerf (P-value = 0.748) and SDI (P-value = 0.080) may indicate that, within this concentration range, the discharge energy (correlated with voltage) primarily defines the channel width and SDI more than the chemical etching rate. Practically, higher KOH concentrations lead to sharper edges (lower roundness) but also rougher surfaces and a higher likelihood of chipping. This highlights a key conflict in optimization: conditions that improve one quality metric may degrade another.

Regarding the quadratic effects, non-linear effects of voltage (V*V) were significant for chipping (P-value = 0.014*), S_a (P-value = 0.0002*), and chipping severity (P-value = 0.0002*), suggesting the negative effects of voltage accelerate non-linearly at higher values.

Table 5
Significance (P-values) of process parameters influencing measured responses is shown. Results identify voltage as the dominant factor affecting all responses ($P < 0.001$), while significant interaction terms (e.g., V × C) and quadratic effects (e.g., S × S) confirm the non-linear nature of the process and necessity of multi-parameter optimization.

Effect Term	P-value					
	Chipping	Cut Kerf	SDI	S_a	Edge Roundness	Chipping Severity (Ordinal) **
Voltage (V)	***<0.001****	***<0.001****	***<0.001****	***<0.001****	***<0.001****	***<0.0001****
Speed (S)	0.222	0.167	***0.023****	***0.008****	0.781	0.0625
KOH Conc. (C)	0.098	0.748	0.080	***0.008****	***0.004****	***<0.0001****
V*V	***0.014****	0.087	0.312	***0.0002****	0.980	***0.0002****
S*S	***0.030****	0.656	0.197	0.726	0.246	***0.0116****
C*C	0.514	***0.001****	***0.017****	0.852	0.965	1.0000
V*S	0.750	0.302	0.861	***0.039****	0.509	0.1155
V*C	0.346	***0.001****	***<0.001****	***<0.001****	0.187	0.9993
S*C	0.540	0.860	0.630	0.794	0.715	0.9997

* Statistically significant (P-value < 0.05).
** P-values for the five continuous responses (chipping through edge roundness) were derived from the REML models. P-values for the chipping severity (ordinal) response were derived from Effect Likelihood Ratio Tests of the OLR model.

Importantly, there appears to be an ideal processing window for speed with respect to chipping, as indicated by the significant S*S terms for both chipping (P-value = 0.030*) and chipping severity (P-value = 0.0116*). In the SACE process, very high machining speeds likely result in tool-workpiece contact causing mechanical breakage and inadequate removal, while too low speeds could cause over-etching or high heat load [33]. This finding highlights a unique feature of SACE optimization compared to traditional methods where slower rates often consistently improve quality [34]. Moreover, significant C*C terms for cut kerf (P-value = 0.001*) and SDI (P-value = 0.017*) indicate complex electrolyte concentration-dependent effects, possibly associated with the influence of electrolyte conductivity on both etching behavior and discharge stability [35].

Interaction terms, like V*C, also significantly influence the results. To fully understand the subsequent interactions, particularly the crucial role of the electrolyte concentration, it is helpful to visualize the proposed specific material removal mechanism during SACE of ion-exchanged aluminosilicate glass (Fig. 6). It is important to note that this figure is a conceptual model based on established principles from the literature, designed to aid in the interpretation of the results. As-received CSG like GG3 (Fig. 6a) features a surface compressive stress layer resulting from the ion-exchange process, where larger K^+ ions replace smaller Na^+ ions within the aluminosilicate glass matrix (compare Fig. 6a and Fig. 6b) [36,37]. During SACE cutting (Fig. 6c), material removal occurs through a synergistic thermochemical action. The sparks generated within the gas film provide intense, localized thermal energy. Simultaneously, the alkaline KOH electrolyte supplies hydroxide (OH^-) ions that chemically attack the glass network structure. This involves the breaking of strong Si-O-Si and Al-O-Si bonds, primarily through the following reactions [35,38].:

$$SiO_2 + 2KOH \rightarrow K_2SiO_3(aq) + H_2O \quad (1)$$

$$Al_2O_3 + 2KOH \rightarrow 2KAlO_2(aq) + H_2O \quad (2)$$

The high local temperatures generated by the discharges significantly accelerate these chemical etching reactions within the spark zone. Another key consideration is that this thermochemical removal occurs within a material containing significant residual stress. The localized energy input from sparks and the material removal process itself can trigger the release of this residual stress [39]. While this stored energy is unlikely to significantly alter the fundamental thermodynamics (e.g., Gibbs free energy) of the chemical etching reactions compared to the high thermal input and chemical potentials involved, its release can interact strongly with the material removal process. Specifically, it can influence micro-crack initiation or propagation from thermally or chemically induced flaws, thereby contributing significantly to phenomena like edge chipping, especially if stresses become unbalanced as material is removed. Therefore, careful optimization of SACE parameters is crucial to mitigate such unwanted defects. Overall, the combined thermal and chemical action leads to accelerated material dissolution and the cutting of the glass, leaving hydroxylated (hydrated) cut surfaces that helps passivate the surface by terminating the glass network (Fig. 6d).

Understanding this mechanism, SACE material removal process, provides critical context for the significant interaction observed between voltage and KOH concentration (V*C) for cut kerf (Fig. 7a), SDI (Fig. 7b), and S_a (Fig. 7c) (P-value ≤ 0.001*). This interaction indicates that the effect of voltage on these responses depends heavily on the KOH concentration. Focusing on S_a (Fig. 7c), the detrimental effect of increasing voltage (leading to higher S_a) is more pronounced at higher KOH concentrations (30 wt.%) compared to lower concentrations (24 wt.%). While higher KOH concentration yields slightly smoother surfaces at low voltage (33V), facilitated by more efficient chemical polishing, it results in significantly rougher surfaces at high voltage (37V). This means that both parameters must be considered simultaneously to achieve a smooth surface. This strong interaction highlights the risk of single-factor optimization and underscores the necessity of the RSM approach. This complex interaction might occur for several reasons. As discussed earlier, a higher electrolyte concentration accelerates chemical etching. At low energy input (low voltage), this faster etching could potentially lead to a smoother surface. However, at high discharge intensities (high voltage), the same rapid chemical attack might worsen surface irregularities, as the powerful discharges generate large fluctuations of hot electrolyte that subsequently lead to a more aggressive and non-uniform etching. Therefore, optimizing SACE cutting for GG3 requires accounting for this interaction. The lack of significance of the V*C interaction for chipping (quantitative P-value = 0.346, ordinal P-value = 0.9993) suggests that while voltage and KOH concentration individually influence chipping severity, their combined effect does not synergistically alter it beyond their additive main and quadratic influences. Chipping appears more strongly driven by the peak discharge energy (related to V and V*V) and non-linear speed effects (S*S), with KOH concentration also playing a direct role in severity.

The V*S interaction was significant only for S_a (P-value = 0.039*). This significance, which is visualized in the interaction plot in Fig. A.2, Appendix A, indicates process trade-offs. The speed that minimizes roughness probability likely depends on the discharge intensity (Voltage). At higher voltages (more aggressive removal), a different speed might be needed to maintain surface quality compared to lower voltages. Finally, the S*C interaction was not significant for any response (P-value ≥ 0.54).

Overall, the analysis confirms voltage as a dominant factor, generally impacting quality negatively at higher levels while determining the intensity of MRR. KOH concentration affects etching efficacy and interacts

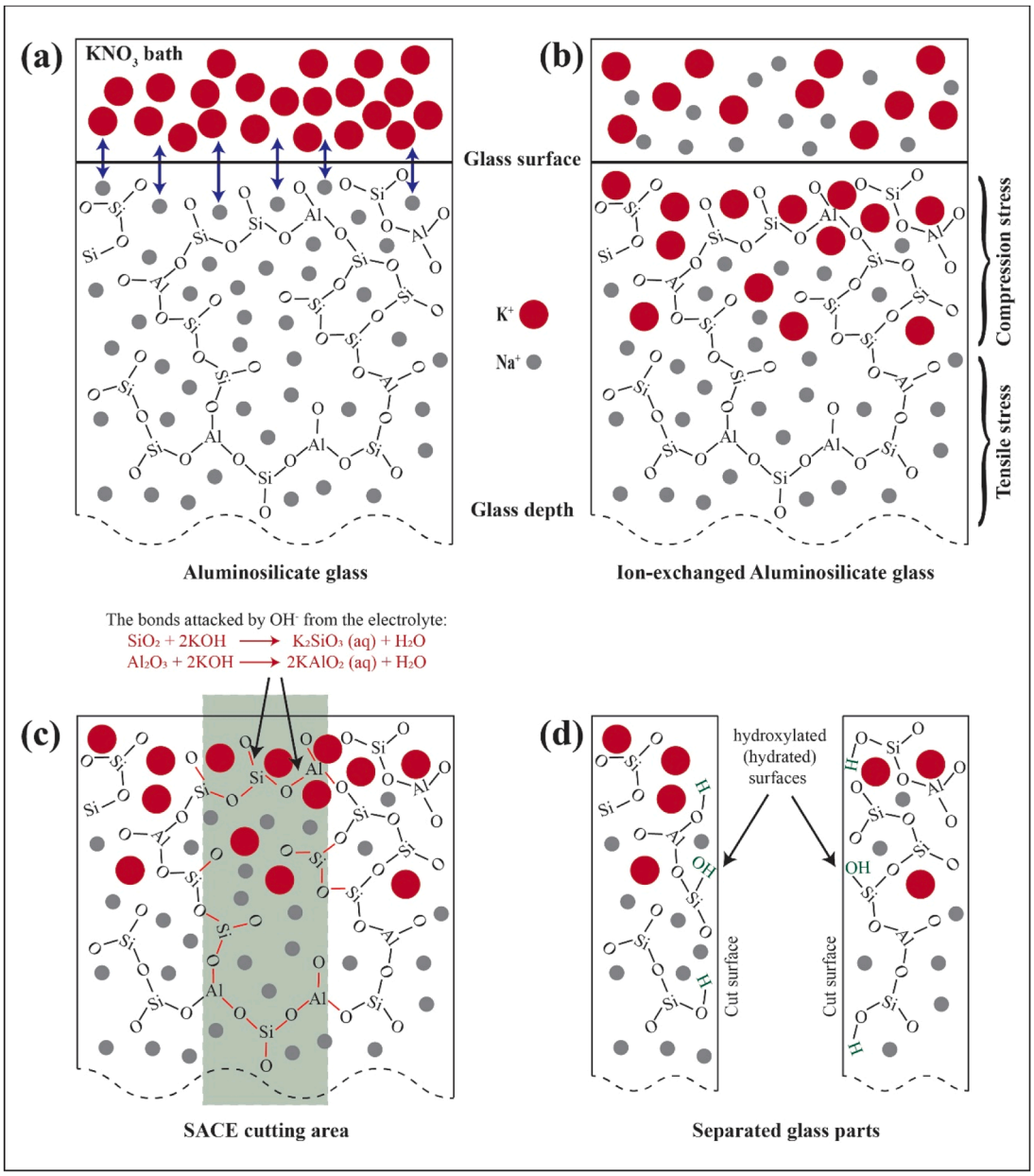

Fig. 6. Proposed SACE mechanism for ion-exchanged aluminosilicate glass, depicting (a) the base structure, (b) the ion-exchanged structure and stress profile, (c) the electrochemical cutting process, and (d) the final separated parts with hydrated surfaces.

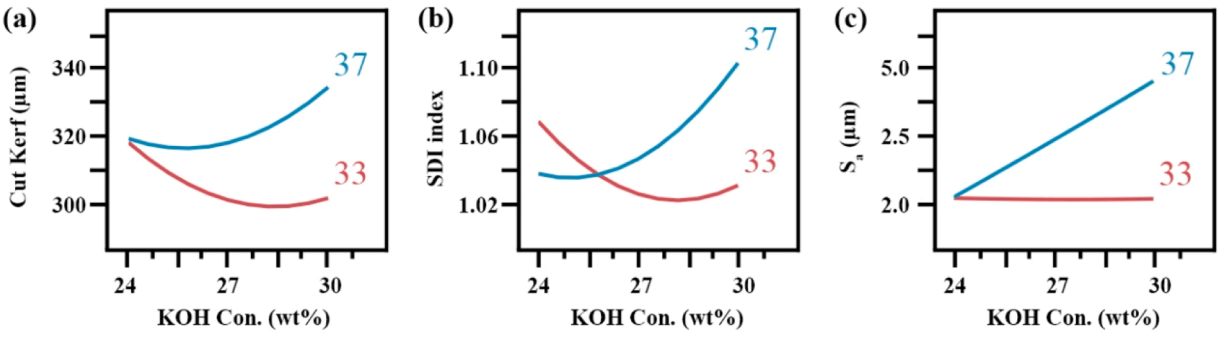

Fig. 7. Interaction profiles illustrate significant interaction effects between voltage and KOH concentration for (a) cut kerf, (b) SDI, and (c) S_a. A synergistic effect is revealed where high voltage degrades surface quality (S_a) and widens the kerf (most pronounced at 30 wt.% electrolyte concentrations).

strongly with voltage, particularly for S_a, cut kerf, and SDI. Speed exhibits significant non-linear effects crucial for chipping control and

interacts with voltage regarding surface roughness. Therefore, optimizing SACE for CSG necessitates balancing these distinct parameter influences and interactions.

3.3. Response surface visualization

Response surface visualization was used to further clarify the complex interactions found between the SACE parameters and the S_a response, which showed the best model fit (R^2Adj = 0.868). Keeping speed constant at its center point (10 μm/s), the response surface plot concentrated on the V*C interaction, which was found to be of utmost importance in the previous section (Table 5, P-value < 0.001).

This 3D response surface graph for S_a is shown in Fig. 8. The plot graphically validates the significant impact of both KOH concentration and voltage. Because of the increased spark intensity and more aggressive machining at higher energy levels [18], the general upward trend along the voltage axis shows that, across the tested KOH concentrations, increasing voltage consistently results in a rougher cut surface (higher S_a). At higher KOH concentrations, the surface roughness increases with voltage more quickly, highlighting the synergistic effect of these two parameters. It should be noted that the surface characteristics may change at different cutting speeds, and that Fig. 8 illustrates the relationship with speed held constant.

In the depicted V-C plane at S = 10 μm/s, the surface does not show a straightforward minimum S_a value, supporting the canonical analysis conclusion that the smoothest surfaces within the overall experimental boundaries are probably located at specific factor limits rather than an interior optimum. This illustration emphasizes how crucial it is to consider both voltage and KOH concentration at the same time to reduce S_a during GG3's SACE production.

3.4. Optimization and prediction

Theoretical optima (minima or saddle points) are located outside the experimentally examined parameter space, according to the canonical analysis of the continuous response surfaces (Section 3.1). This result suggests that within the tested ranges of SACE parameters (Table 3), the optimal result for any single response (e.g., the absolute minimum S_a or SDI closest to 1) most likely occurs at the boundaries of this process window, i.e., at the lowest or highest settings of one or more parameters. Since multiple combinations of parameters across the tested range can yield acceptable SACE cutting results, the most suitable process depends on the particular application.

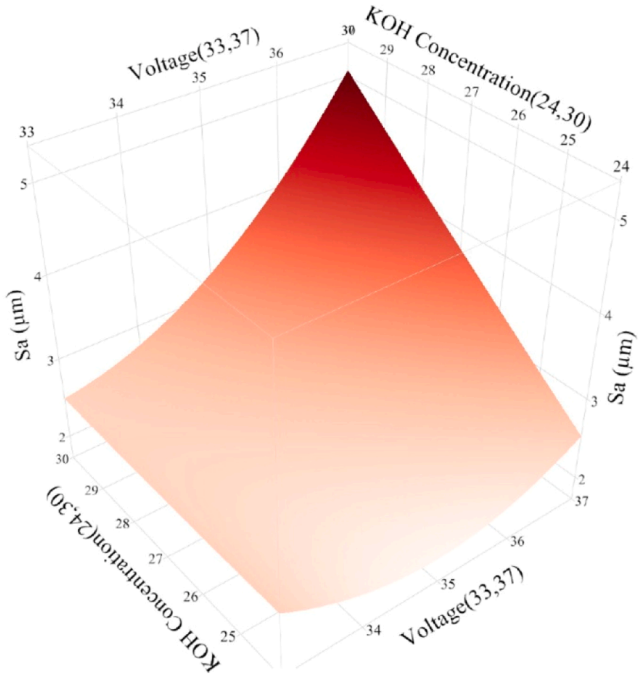

Fig. 8. Predicted S_a (μm) as a function of voltage and KOH concentration (Speed held constant at 10 μm/s) is visualized. Optimal surface smoothness is achieved at process window boundaries (lower voltage) rather than a central optimum, indicated by the steep gradient toward the high-voltage/high-concentration corner.

A useful tool for this investigation is the prediction profiler [40]. As each factor is changed, it interactively shows the anticipated values for all fitted response models at once, allowing the visualization of parameter sensitivity and contradictory response trends. Additionally, based on specific goals, e.g., minimize, maximize, target a value, each response can be assigned to a desirability function, i.e., a mathematical function that assigns a value between 0 and 1 based on how well a given setting meets a specific goal. These functions can then be combined into an overall desirability score to numerically search for the parameter combination offering the best overall compromise.

The projected results for the continuous responses are displayed in Fig. 9 for the prediction profiler set at a representative operating point (V = 35 V, S = 10 μm/s, C = 27 wt.%). The expected results under these center-point conditions are roughly as follows: edge roundness ≈ 6.8 μm, S_a ≈ 2.6 μm, cut kerf ≈ 307 μm, SDI ≈ 1.03, and chipping ≈ 4.1 μm. The slopes of the profile lines visually confirm the significant parameter effects identified in Section 3.2. For example, increasing voltage clearly increases predicted cut kerf and S_a, while decreasing SDI and edge roundness. This outcome aligns with its strong main effects (Table 4). A trade-off is evident when speed increases, as there is a small drop in cut kerf but an increase in SDI. The effect of increased KOH concentration includes a notable decrease in roundness and an increase in S_a.

The overall desirability at the center point is calculated as 0.63, assuming the objectives are to minimize all continuous responses towards 1, indicating a reasonably good, but not perfect, compromise between the competing quality objectives. In the current experimental space, the highest desirability of 0.79 was obtained at the operating point of V = 33 V, S = 5 μm/s, C = 30 wt.%, as shown in Fig. A.3, Appendix A.

3.5. Visual confirmation and process demonstration

To visually evaluate the results, the cut edges and cut surfaces produced under various SACE parameters were examined using optical imaging systems as explained in Section 2.3. Representative micrographs are shown in Fig. 10 (cut edge) and Fig. 11 (cut surface).

Fig. 10 presents top-down edges of the SACE cut (see Fig. 5 for the top and bottom edge definitions), allowing for a comparison of how different processing conditions impact edge quality and chipping. For example, Fig. 10a and b—obtained at high V = 37 V with moderate S (10 μm/s) and C (27 wt.%)—show levels of edge irregularity comparable to those in Fig. 10c and d, which were produced at high C (30 wt.%), also with moderate V (35 V) and S (10 μm/s). Under both parameter sets, the top cut edge clearly exhibits better quality than the bottom edge. This difference can likely be attributed to superior electrolyte flow in the top region, which enhances both the chemical etching aspect of the process and the stability of the sparks. Since higher electrolyte concentrations also increase viscosity, this change could affect local flow. Such viscosity-influenced flow differences might then explain why the edge roundness varies between the top and bottom surfaces.

The synergistic effect of the SACE parameters is evident in Fig. 10e and f, where V, S, and C were all set to their maximum values. These conditions resulted in widespread chipping, clearly visible on both sides of the cut.

Regarding chipping, it should also be kept in mind that, particularly for GG3 and other CSGs, not all instances can be solely attributed to the machining parameters. As shown in Fig. 4, residual stress is present within this glass. An imbalance between the compressive stress near the

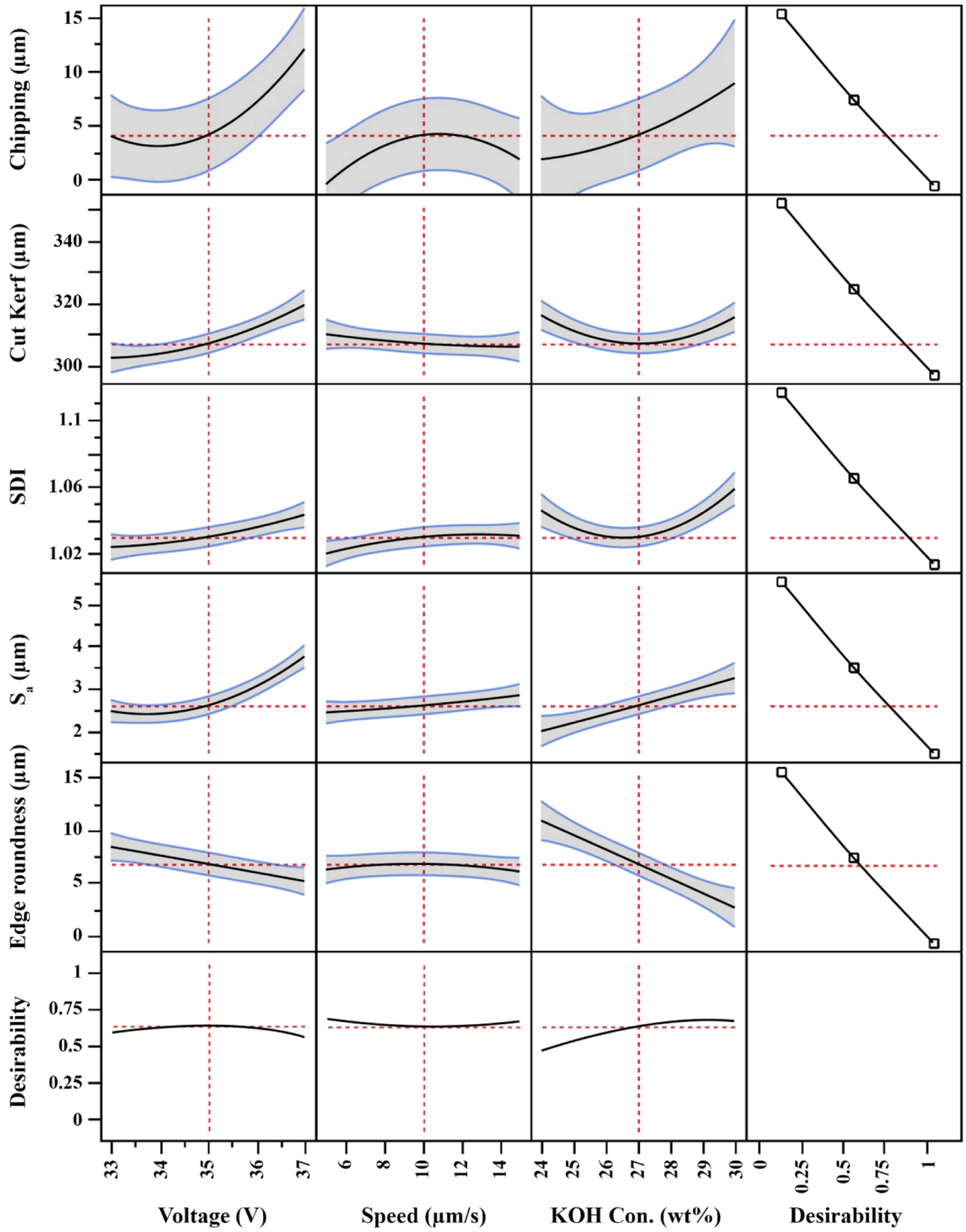

Fig. 9. Predicted values and desirability functions at the center operating point (V = 35 V, S = 10 µm/s, C = 27 wt.%) are illustrated. Critical trade-offs are demonstrated by slopes (increased voltage improves edge roundness but worsens chipping and surface roughness) resulting in moderate desirability (0.63).

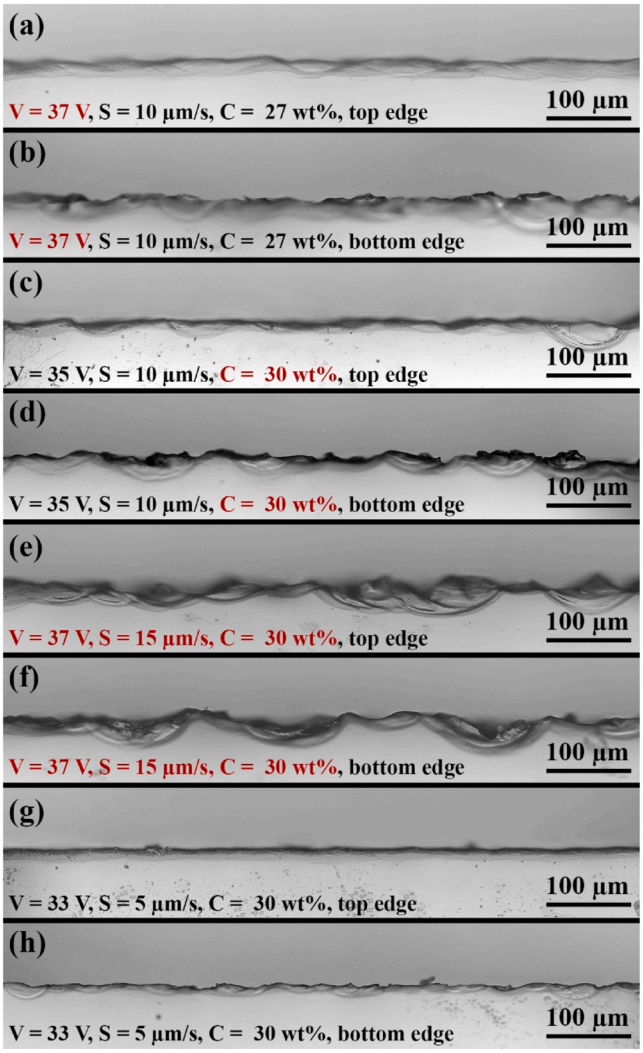

Fig. 10. Optical micrographs showing examples of SACE cut edges obtained under various machining parameters: (a, b) S_a = 3.73 μm; V = 37 V, S = 10 μm/s, C = 27 wt.%, (c, d) S_a = 2.65 μm; V = 35 V, S = 10 μm/s, C = 30 wt.%, (e, f) S_a = 5.26 μm; V = 37 V, S = 15 μm/s, C = 30 wt.%, and (g, h) S_a = 2.41 μm; V = 33 V, S = 5 μm/s, C = 30 wt.% (see Fig. 5 for the top and bottom edge definitions).

surfaces and the internal tensile stress can lead to uncontrolled fracture. While the dissolution of the glass structure during the SACE process can significantly mitigate this inherent issue, suboptimal conditions—such as insufficient electrolyte reaching the bottom edge—can worsen chipping. This is potentially because the processing fails to adequately relieve or manage these stresses.

By contrast, when optimal parameters are employed that allow sufficient time and flow for the electrolyte to reach the bottom edge effectively, acceptable cutting quality can be achieved on both top and bottom surfaces. This is demonstrated in Fig. 10g and h, which represents the most desirable overall cut quality observed throughout the experiments, achieving good results on both edges.

Fig. 11 shows the cut surface topography, from which the S_a values were measured. The surfaces shown in Fig. 11a and b, which correspond to parameter conditions where only V or C was set to an extreme value (related to cut edges in Fig. 10a-d), exhibit a smoother texture compared to the surface shown in Fig. 11c. The latter was generated using the maximum parameter settings (related to edges in Fig. 10e and f), highlighting the significant impact of parameter interactions, especially V*C, on S_a. Consistent with the edge quality observations, the lowest S_a value (Fig. 11d) among these conditions was obtained for the surface corresponding to the optimal cut edges shown in Fig. 10g and h. Furthermore, significant electrolyte etching effects are visible, particularly near the top surface cut edge regions at high KOH concentrations (Figs. 11b and 11d). Their prominence in Figs. 11b and 11d, compared to Figs. 11a and 11c, is attributed to the enhanced chemical reactivity of the electrolyte at higher concentrations and simultaneously at low to moderate cutting speeds. This localized etching phenomenon is particularly effective on the top surface, as visually apparent in the smoother texture of the top sections of Figs. 11b and 11d when compared to their respective bottom sections. This enhanced etching is facilitated by superior electrolyte flow on the top surface, which leads to better removal of reaction products and consistent chemical attack. Consequently, this phenomenon significantly contributes to a considerable reduction in the overall measured S_a value in some samples, notably resulting in the lower S_a of 2.41 μm in Fig. 11d, where these effects are maximized.

Finally, to demonstrate the practical capability and stability of the SACE process for creating extended, non-linear features using optimally selected parameters, a long spiral cut was produced (Fig. 12). The parameters chosen for this demonstration (V = 33 V, S = 5 μm/s, C = 30 wt.%) represent conditions identified as having the best desirability factor (as explained in Section 3.4). The resulting cut shown in Fig. 12 displays a consistent width and smooth curvature over an extended path, with minimal visible edge defects. This successful demonstration validates the potential of the SACE process, guided by RSM optimization, for reliably producing defined freeform features in GG3 glass for potential repurposing applications.

Regarding industrial scalability and throughput, the optimal cutting speed of 5 μm/s through 550 μm-thick GG3 represents a trade-off between achieving high quality and processing time. While this speed is suitable for high-value, precision applications, it is important to view this limitation in the context of competing technologies. For instance, femtosecond (fs) laser setups often involve high investment costs and complex operational requirements, making them less straightforward to implement in many production environments. In contrast, SACE operates on principles similar to typical CNC machining, utilizing standard G-codes, which allows it to be integrated more easily into existing production processes. This relative accessibility makes SACE a compelling option despite its current speed. To enhance its economic viability for larger-scale production, future work should still explore methods to increase the material removal rate, such as using multi-tool arrays.

Beyond scalability, process stability and long-term tool wear are essential for industrial adoption. The fundamental difference in wear mechanism provides SACE a distinct advantage over conventional mechanical machining of CSG. Mechanical processes (e.g., electroplated diamond drilling [13]) require physical abrasion to fracture the high-hardness surface compression layer, resulting in rapid tool wear and inconsistent hole quality. In this study, the tool wear was negligible, a characteristic intrinsic to the SACE mechanism. As described in SACE literature [41,42], a stable gas film forms around the tool electrode acting as a hydrodynamic barrier physically isolating the metal electrode from the glass workpiece, thereby shielding the tool from mechanical abrasion. This theoretical stability was confirmed experimentally by the successful fabrication of a long, continuous spiral cut (Fig. 12), which maintained consistent cut width and geometry over an extended path without observed cutting performance reduction or tool failure. Although minor tool wear caused by thermal evaporation or chemical attack during discharge can occur, it is significantly lower than the severe abrasive wear observed in mechanical drilling, particularly for WC tool electrodes due to their high thermal resistance. No significant change in the WC electrode geometry was observed within the stable process window, confirming that SACE provides a stable non-contact machining environment where tool life is determined by thermal management rather than the hardness of the CSG substrate.

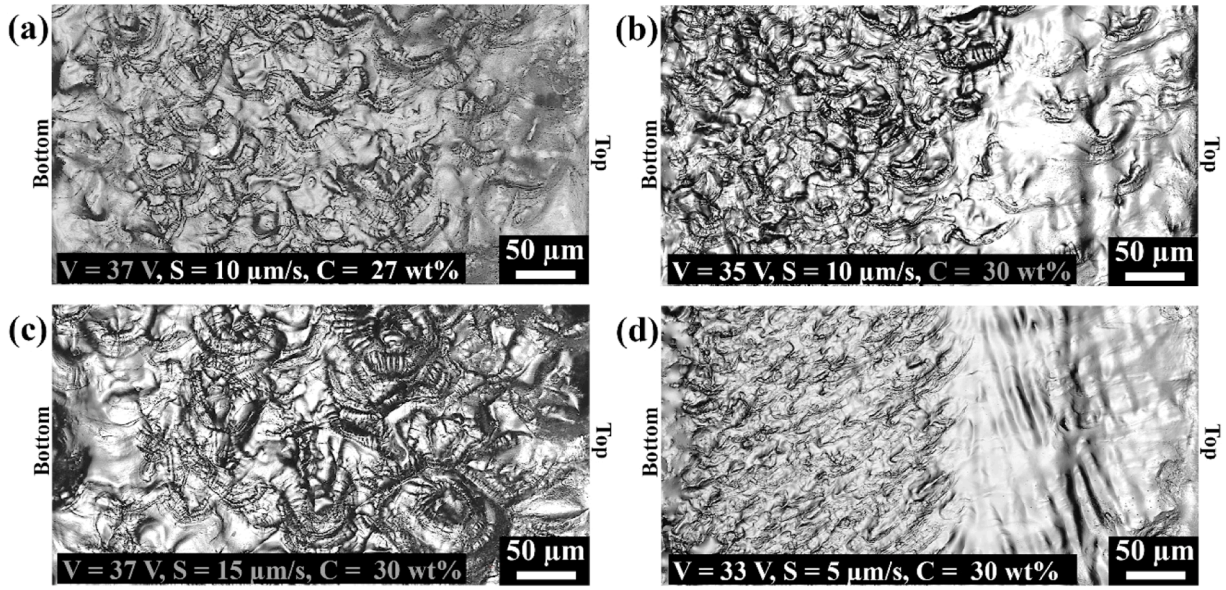

Fig. 11. Optical micrographs showing examples of cut edge surface topography (related to S_a) under various machining parameters: (a) $S_a = 3.73$ µm; V = 37 V, S = 10 µm/s, C = 27 wt.%, (b) $S_a = 2.65$ µm; V = 35 V, S = 10 µm/s, C = 30 wt.%, (c) $S_a = 5.26$ µm; V = 37 V, S = 15 µm/s, C = 30 wt.%, and (d) $S_a = 2.41$ µm; V = 33 V, S = 5 µm/s, C = 30 wt.% (see Fig. 5 for the top and bottom edge definitions).

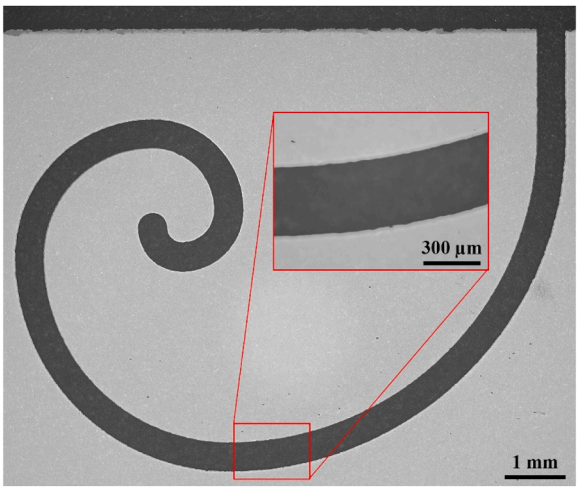

Fig. 12. Macroscopic view of a long spiral cut demonstrating SACE process capability on GG3 using optimized parameters (V = 33 V, S = 5 µm/s, C = 30 wt.%) is presented. Ability to produce complex freeform geometries with consistent width and minimal defects is visually confirmed.

3.6. Comparative benchmarking

Benchmarking optimized results against mechanical, laser, and hybrid techniques demonstrates the potential of SACE for CSG micro machining. Performance metrics including inlet chipping, surface roughness, geometric freedom, and approximate cost— capital expenditure (CapEx) and operational expenses—for each machining technique are summarized in Table 6.

SACE occupies a unique manufacturing niche by offering high-quality freeform fabrication at a moderate price. Fs laser technique remains the benchmark for mirror-like surface finish and high throughputs (up to 40 mm/s), but accessibility is restricted by high capital costs and optical complexity. Furthermore, laser methods are primarily strictly directional tools which struggle to fabricate complex 2.5D blind features or non-linear pockets without extensive taper or thermal damage. CO_2 laser cleavage requires a two-step process where rapid final separation via thermal shock (5-90 mm/s) necessitates a significantly slower preparatory groove fabrication step (0.5-2 mm/s). This technique is typically limited to linear separation and lower edge quality (top surface $R_z \approx 21$ µm) compared to the single-step freeform capabilities of SACE. Mechanical methods such as ultrasonic milling and diamond drilling fall within a similar price range to SACE (low to medium) but suffer from severe edge integrity issues due to internal stress. Optimized ultrasonic milling results in inlet chipping (~50-100 µm) significantly larger than the 4.1 µm achieved by SACE.

Although single-tool SACE cutting speed (0.005 mm/s) is lower than laser-based mass production techniques, this limitation is mitigated through parallel scalability (Section 3.7). The process provides a strategic advantage for high-value, low-volume prototyping as it delivers edge quality comparable to high-end lasers (chipping < 5 µm) with the geometric versatility of milling (2.5D features) at a medium cost significantly lower than fs laser systems (high cost).

3.7. Engineering applications

Machining of CSG without catastrophic fracture is demonstrated by SACE, enabling three critical engineering applications. *Post-process modification* is facilitated for direct creation of sensor ports and camera openings in standard commercial ion-exchanged glass panels. While thermal stress cleavage is restricted to straight cuts starting from an edge, complex 2.5D geometries and internal features with tight curves are generated by SACE. *Freeform microfluidics* are supported as a cost-effective alternative to expensive laser systems for creation of blind pockets and non-linear channels. Utilization of thermally accelerated chemical etching rather than mechanical force avoids release of internal stress associated with shattering in traditional drilling, rendering the method suitable for high-pressure microfluidic devices.

A key advantage of SACE regarding industrial adoption is its potential for parallel scalability. Unlike mechanical drilling requiring complex independent spindles, SACE is driven by a thermochemical material removal mechanism, allowing utilization of multi-electrode arrays (e.g., 5 × 5 tool grids) on a single Z-axis stage for simultaneous machining of multiple features. Limitation of single-tool cutting speed (5 µm/s) is mitigated by linear scaling of material removal rate with electrode count, rendering the process viable for high-throughput applications such as glass interposer fabrication.

Table 6
Comparative benchmarking of SACE against other alternative CSG machining techniques.

Machining Technique	Mechanism	Inlet Chipping (μm)	Surface Roughness (μm)	Geometric Freedom	Speed (Feed Rate) (mm/s)	System Cost*	Source
SACE (Lab-Scale)	Thermochemical etching	4.1	2.41 (S_a)	High (2.5D freeform, blind pockets/ channels)	0.005	Medium	Current work
CO_2 Laser Cleavage	Fracture control via thermal shock	–	~21 (top surface) ~2 (center) (R_z)	Low (mainly linear separation)	0.5-2 (groove fabrication scan rate) 5-90 (cleavage scan rate)	Low	[8]
Femtosecond Laser Pulse Irradiation	Sub-surface crack propagation	–	0.01 (R_{Sm})	Medium (linear and curved separation)	5-40	High	[10]
Ultrasonic-Vibration-Assisted Helical Milling	Micro-fracture control	~50-100	–	High (2.5D/3D features)	1.33	Medium	[12]
Diamond Drilling	Mechanical abrasion/ grinding	~20	–	Low (holes only)	0.0167	Low	[13]
Hybrid Electrochemical Discharge (ECD) and Grinding	Thermal/chemical erosion + mechanical abrasion	–	–	Medium (linear cutting/channels)	0.01-0.05 (ECD) – (grinding)	Medium	[15]

* Cost includes CapEx and operational expenses.

Finally, *circular economy frameworks* are enabled by these low-damage characteristics, permitting high-value upcycling of glass waste (discarded smartphone screens) into functional optical components without extensive post-process grinding.

4. Conclusion and outlook

This research establishes the first successful implementation of SACE for the freeform machining of CSG, proving it to be a superior processing route compared to conventional and laser-based methods. The results confirm that SACE effectively overcomes the catastrophic chipping issues inherent to CSG, yielding cut qualities that outperform existing techniques in a single-step process. This investigation additionally discloses novel perspectives on the SACE machining process by means of a comprehensive DOE analysis, where the equilibrium of various process setting effects was evaluated for critical metrics, including chipping, S_a, cut kerf, SDI, and edge roundness. The RSM optimized SACE parameters significantly affected cut quality properties and demonstrated complex interactions between voltage, cutting speed and KOH concentration.

Specifically, this work defined a robust and statistically validated process window for the machining of GG3. A REML technique was used for model fitting. Although the model showed only moderate predictive capabilities (R^2 Adj ≈ 0.54 for chipping)—a common challenge when machining brittle materials due to inherent process stochasticity—this technique proved essential for process optimization. The JMP prediction profiler tool enabled the determination of an optimal parameter set (V = 33 V, S = 5 μm/s, C = 30 wt.%) that produced an overall desirability of 0.79, and under these conditions, high-quality cuts with minimal chipping (~4.1 μm) and a smooth surface finish (Sa ≈ 2.41 μm) were achieved. The results highlight the significant impact of voltage (P-value < 0.001), the combined effect of voltage and KOH concentration, and the importance of the quadratic effect of machining speed on chipping, as demonstrated by S*S terms for both chipping (P-value = 0.030) and chipping severity (P-value = 0.0116). Furthermore, this research illuminated the challenge of simultaneously minimizing both chipping and edge roundness owing to competing parameter effects. The optimized SACE process delivers its primary benefit by solving the main CSG machining problem, which is catastrophic chipping caused by high surface compressive stress. This thermochemical method outperforms mechanical and laser techniques by enabling controlled material removal with reduced defects while other methods produced larger chipping or needed multiple processing steps.

These findings possess considerable practical significance for the circular economy because the method enables the re-machining of high-value CSG waste such as smartphone screens into customized optical components, thereby diverting these materials from landfills.

Notwithstanding these promising results, this study exhibits several limitations that present evident paths for subsequent research. The optimal cutting speed of 5 μm/s introduces a clear trade-off with industrial throughput, and the process optimum might exist at the boundaries of the explored parameter range. Moreover, long-term tool performance was not a primary focus. Future research requires further investigation of electrode wear and scalability to resolve the gap between laboratory success and industrial implementation. The research should expand its experimental design to study various parameters while testing different tool shapes, rotation speeds, and implementing real-time monitoring systems for better process management. Additionally, researchers might investigate pulsed-DC power supplies to evaluate their impact on the stability and efficiency of the SACE process, because this technology can improve spark stability and gas film uniformity, which potentially facilitates higher material removal rates at lower voltages while reducing thermal damage. The investigation of alternative electrolytes, such as surfactant-enhanced electrolytes, is also justified to determine if a varied equilibrium of chemical reactivity and conductivity might result in an expansion of the stable processing window. Furthermore, a dedicated study concerning advanced tool geometries, which include hollow or internally fluted electrodes, should be conducted to evaluate the hypothesis that enhanced electrolyte flushing could improve surface quality at increased speeds. These experimental endeavors could subsequently be combined with finite element modeling (FEM) to more accurately predict the thermal and chemical gradients present at the tool-workpiece interface, which would lead to a more robust and physics-based understanding of the SACE process for CSG.

Declaration of generative AI and AI-assisted technologies in the writing process

During the preparation of this work the authors used Gemini Pro 2.5 model in order to assist with grammar, spelling, punctuation, and overall sentence structure, enhancing the clarity and flow of the text. After using this tool/service, the authors reviewed and edited the content as needed and take full responsibility for the content of the published article.

CRediT authorship contribution statement

Seyed Ali Delbari: Writing – review & editing, Writing – original

draft, Visualization, Validation, Software, Methodology, Investigation, Formal analysis, Data curation, Conceptualization. **Jean-Philippe Leclair:** Writing – review & editing, Visualization, Methodology, Investigation, Data curation, Conceptualization. **Guillaume Villeneuve:** Writing – review & editing, Visualization, Methodology, Investigation, Data curation, Conceptualization. **Lucas A. Hof:** Writing – review & editing, Validation, Supervision, Resources, Project administration, Methodology, Funding acquisition, Conceptualization.

Declaration of competing interest

The authors declare that they have no known competing financial interests or personal relationships that could have appeared to influence the work reported in this paper.

Acknowledgements

The authors gratefully acknowledge the Natural Sciences and Engineering Research Council of Canada (NSERC) under the Discovery Grant (RGPIN-2019-05973), and the Québec Circular Economy Research Network (RRECQ) for their financial support enabling this project.

Supplementary materials

Supplementary material associated with this article can be found, in the online version, at doi:10.1016/j.rineng.2026.109591.

Data availability

Data will be made available on request.

References

[1] R. Rajaramakrishna, J. Kaewkhao, Glass Material and their Advanced Applications, KnE Social Sciences, 2019, https://doi.org/10.18502/kss.v3i18.4769.
[2] J.H. Butler, P.D. Hooper, G. Waste, Waste: a handbook for management, Elsevier (2019) 307–322, https://doi.org/10.1016/B978-0-12-815060-3.00015-3.
[3] M. Zier, P. Stenzel, L. Kotzur, D. Stolten, A review of decarbonization options for the glass industry, Energy Convers. Manag.: X 10 (2021) 100083, https://doi.org/10.1016/j.ecmx.2021.100083.
[4] T. Ahmed, M. Ali, U. Akmal, F. Aslam, W. Abbass, M. Aziz, M. Hamza, I. Shah, H. A. Shah, Coupled effect of waste glass powder and glass fibers on mechanical properties of concrete: A step towards the elimination of non-biodegradable waste, Struct. Concr. 24 (2023) 7603–7624, https://doi.org/10.1002/suco.202201000.
[5] O. Adekomaya, T. Majozi, Mitigating environmental impact of waste glass materials: review of the existing reclamation options and future outlook, Environ. Sci. Pollut. Res. 28 (2021) 10488–10502, https://doi.org/10.1007/s11356-020-12263-0.
[6] S. Berneschi, G.C. Righini, S. Pelli, Towards a glass New world: the role of ion-exchange in modern technology, Appl. Sci. 11 (2021) 4610, https://doi.org/10.3390/app11104610.
[7] T. Bristogianni, F. Oikonomopoulou, Glass up-casting: a review on the current challenges in glass recycling and a novel approach for recycling “as-is” glass waste into volumetric glass components, Glass. Struct. Eng. 8 (2023) 255–302, https://doi.org/10.1007/s40940-022-00206-9.
[8] T. Furumoto, Y. Hashimoto, H. Ogi, T. Kawabe, M. Yamaguchi, T. Koyano, A. Hosokawa, CO2 laser cleavage of chemically strengthened glass, J. Mater. Process. Technol. 289 (2021) 116961, https://doi.org/10.1016/j.jmatprotec.2020.116961.
[9] H. Ogi, T. Furumoto, T. Koyano, A. Hosokawa, Study on thermal stress cleavage of chemically strengthened glass by CO2 laser beam, Procedia CIRP. 42 (2016) 460–463, https://doi.org/10.1016/j.procir.2016.02.232.
[10] S. Park, Y. Kim, J. You, S.-W. Kim, Damage-free cutting of chemically strengthened glass by creation of sub-surface cracks using femtosecond laser pulses, CIRP Ann. 66 (2017) 535–538, https://doi.org/10.1016/j.cirp.2017.04.071.
[11] C.-F. Chuang, K.-S. Chen, T.-C. Chiu, T.-S. Yang, M.-C. Lin, Crafting interior holes on chemically strengthened thin glass based on ultrafast laser ablation and thermo-shock crack propagations, Sens. Actuators Phys. 301 (2020) 111723, https://doi.org/10.1016/j.sna.2019.111723.
[12] K. Noma, Y. Takeda, T. Aoyama, Y. Kakinuma, S. Hamada, High-precision and High-efficiency micromachining of chemically strengthened glass using ultrasonic vibration, Procedia CIRP. 14 (2014) 389–394, https://doi.org/10.1016/j.procir.2014.03.107.
[13] A. Mizobuchi, Y. Kagawa, T. Ishida, Miniature drilling of chemically strengthened glass plate using electroplated diamond tool, Int. J. Autom. Technol. 10 (2016) 780–785, https://doi.org/10.20965/ijat.2016.p0780.
[14] K. Noma, Y. Kakinuma, T. Aoysma, S. Hamada, Ultrasonic vibration-assisted machining of chemically strengthened glass with workpiece bending, J. Adv. Mech. Des. Syst. Manuf. 9 (2015), https://doi.org/10.1299/jamdsm.2015jamdsm0016. JAMDSM0016–JAMDSM0016.
[15] J. Kim, J. Hwang, Cutting of chemically strengthened glass using the combination of electrochemical discharge and grinding processes, J. Korean Soc. Precis. Eng. 41 (2024) 957–964, https://doi.org/10.7736/JKSPE.024.096.
[16] H. Müller, S. Henkel, C. Schulze, S. Frank, J. Bliedtner, T. Arnold, Freeform surfaces manufactured with a combination of ultra-fine grinding and plasma jet polishing, J. Eur. Opt. Soc.-Rapid Publ. 21 (2025) 12, https://doi.org/10.1051/jeos/2025007.
[17] Z. Sun, S. To, K.M. Yu, An investigation in the ultra-precision fly cutting of freeform surfaces on brittle materials with high machining efficiency and low tool wear, Int. J. Adv. Manuf. Technol. 101 (2019) 1583–1593, https://doi.org/10.1007/s00170-018-3013-7.
[18] L.A. Hof, R. Wuthrich, Glass precision micro-cutting using spark assisted chemical engraving, Adv. Ind. Manuf. Eng. 3 (2021) 100056, https://doi.org/10.1016/j.aime.2021.100056.
[19] A. Doke, A.M. Badadhe, P. Dixit, Enhancing the borosilicate glass micromachining by using mixed alkaline electrolytes in the ECDM process, Mater. Manuf. Process 39 (2024) 1224–1235, https://doi.org/10.1080/10426914.2024.2311393.
[20] S.M. Seyedi Sahebari, Z. Bassyouni, A. Barari, J.D. Abou Ziki, Intelligent characterization of spark-assisted chemical engraving (SACE) process using time series classification, Int. J. Adv. Manuf. Technol. 130 (2024) 945–960, https://doi.org/10.1007/s00170-023-12692-4.
[21] V. Rajput, M. Goud, N.M. Suri, S. Grover, S. Singh, S. Kumar, Investigation on glass material’s hole characteristics using different tool geometries in cognitive electrochemical discharge machining process, J. Mater. Eng. Perform. (2025), https://doi.org/10.1007/s11665-025-10685-w.
[22] G. Villeneuve, L.A. Hof, On the use of the current signal in spark assisted chemical engraving for micromachining process control, Precis. Eng. 83 (2023) 181–191, https://doi.org/10.1016/j.precisioneng.2023.06.007.
[23] G. Villeneuve, L.A. Hof, SACETraj: an AutoCAD Catmull-rom spline trajectory interpolator, SoftwareX. 27 (2024) 101794, https://doi.org/10.1016/j.softx.2024.101794.
[24] R. Wüthrich, L.A. Hof, The gas film in spark assisted chemical engraving (SACE)—A key element for micro-machining applications, Int. J. Mach. Tools. Manuf. 46 (2006) 828–835, https://doi.org/10.1016/j.ijmachtools.2005.07.029.
[25] R. Gilliam, J. Graydon, D. Kirk, S. Thorre, A review of specific conductivities of potassium hydroxide solutions for various concentrations and temperatures, Int. J. Hydrog. Energy 32 (2007) 359–364, https://doi.org/10.1016/j.ijhydene.2006.10.062.
[26] L. Hof, X. Guo, M. Seo, R. Wüthrich, J. Greener, Glass imprint templates by Spark assisted chemical engraving for microfabrication by hot embossing, Micromachines 8 (2017) 29, https://doi.org/10.3390/mi8010029.
[27] M.J. Anderson, P.J. Whitcomb, RSM Simplified, Productivity Press, 2016, https://doi.org/10.1201/9781315382326.
[28] D.C.. Montgomery, Design and analysis of experiments, John Wiley & Sons, Inc., 2013.
[29] R. Wüthrich, V. Fascio, Machining of non-conducting materials using electrochemical discharge phenomenon—An overview, Int. J. Mach. Tools. Manuf. 45 (2005) 1095–1108, https://doi.org/10.1016/j.ijmachtools.2004.11.011.
[30] V. Rajput, M. Goud, N.M. Suri, Machinability study of Spark assisted chemical engraving (SACE): a state of art, Ind. Eng. J. 52 (2023) 2493–2515.
[31] C.T. Yang, S.S. Ho, B.H. Yan, Micro hole machining of borosilicate glass through electrochemical discharge machining (ECDM), Key. Eng. Mater. 196 (2001) 149–166, https://doi.org/10.4028/www.scientific.net/KEM.196.149.
[32] G. Zhu, H. Li, W. Lu, S. Liu, W. Liu, Y. Zhao, Inducing electrochemical discharges on insulating surfaces for damage-free electrochemical jet machining of glass, Int. J. Mach. Tools. Manuf. 209 (2025) 104293, https://doi.org/10.1016/j.ijmachtools.2025.104293.
[33] M. Harugade, S. Waigaonkar, N. Mane, N. Hargude, Experimental investigation of high speed tool rotation on heat affected zone and over cut in ECDM, mater, Today Proc. 18 (2019) 1472–1478, https://doi.org/10.1016/j.matpr.2019.06.616.
[34] T.G. Bifano, T.A. Dow, R.O. Scattergood, Ductile-regime grinding: A new technology for machining brittle materials, J. Eng. Ind. 113 (1991) 184–189, https://doi.org/10.1115/1.2899676.
[35] S. Sharma, T. Singh, A. Dvivedi, A review on developments in electrolytes and their feeding methods for ECDM process, Silicon (2022), https://doi.org/10.1007/s12633-022-02134-3.
[36] J.-E. Broquin, S. Honkanen, Integrated Photonics on Glass: A review of the ion-exchange technology achievements, Appl. Sci. 11 (2021) 4472, https://doi.org/10.3390/app11104472.
[37] H. Sun, R. Dugnani, Precise residual stress profile in ion-exchanged silicate glass by modified contour method, J. Eur. Ceram. Soc. 41 (2021) 4355–4368, https://doi.org/10.1016/j.jeurceramsoc.2021.02.034.
[38] V.A. Pokrovskii, H.C. Helgeson, Thermodynamic properties of aqueous species and the solubilities of minerals at high pressures and temperatures: the system Al2O3-H2O-KOH, Chem. Geol. 137 (1997) 221–242, https://doi.org/10.1016/S0009-2541(96)00167-2.
[39] M. Wang, L. Jiang, X. Li, J. Liu, J. Li, Y. Yan, Structure and mechanical response of chemically strengthened aluminosilicate glass under different post-annealing conditions, J. Non. Cryst. Solids. 554 (2021) 120620, https://doi.org/10.1016/j.jnoncrysol.2020.120620.

[40] B. Jones, The prediction profiler at 30, Qual. Eng. 33 (2021) 417–424, https://doi.org/10.1080/08982112.2021.1874015.
[41] A. Behroozfar, M.R. Razfar, Experimental study of the tool wear during the electrochemical discharge machining, Mater. Manuf. Process 31 (2016) 574–580, https://doi.org/10.1080/10426914.2015.1004685.
[42] S. Mahmoud, S. Sahebari, Thesis, University of Ontario Institute of Technology, 2025.